



Stabilizing conversion reaction electrodes by MOF derived N-doped carbon shell for highly reversible lithium storage

Fang Liu^{a,b}, Shiyu Liu^a, Jiashen Meng^a, Fanjie Xia^{a,b}, Zhitong Xiao^a, Ziang Liu^a, Qi Li^{a,**}, Jinsong Wu^{a,b,*}, Liqiang Mai^a

^a State Key Laboratory of Advanced Technology for Materials Synthesis and Processing, Wuhan University of Technology, Wuhan, 430070, China

^b Nanostructure Research Centre (NRC), Wuhan University of Technology, Wuhan, 430070, China

ARTICLE INFO

Keywords:

MOF shell
Low-temperature melting synthesis
Carbon-confined nanostructure
In situ transmission electron microscopy
Lithium-ion battery

ABSTRACT

Surface engineering has been applied to resolve the problem of cycling instability in conversion/alloying reaction electrodes which can have high capacity but suffer from large volumetric change and pulverization in electrochemical cycles. However, due to structural instability, most of the surface coatings are still fragile and unstable in electrochemical cycles. Here, a facile low-temperature melting method has been developed to fabricate a uniform and ultrathin metal-organic framework (MOF) shell on various oxides electrode materials, followed by a gradient heat treatment process. A uniform and ultrathin N-doped carbon (NC) shell is formed as a robust coating to keep the integrity of materials and provide a highly conductive pathway for both electron and ions. This carbon confinement strategy can be easily applied to diverse ternary metal oxides with high bonding energy, such as Zn_2SiO_4 , Zn_2WO_4 and Zn_2TiO_4 . The obtained carbon-confined Zn_2SiO_4 ($Zn_2SiO_4@NC$) nanowires have achieved enhanced lithium storage performances compared to pure Zn_2SiO_4 nanowires. As revealed by *in situ* transmission electron microscopy, in the process of lithiation the $Zn_2SiO_4@NC$ nanowires have lower radical expansion and faster kinetics than pure Zn_2SiO_4 nanowires, and the N-doped carbon shell remains stable. This work provides a new approach for the design and construction of carbon-based nanostructures which have great potential in energy-related applications.

1. Introduction

Surface engineering, *i.e.*, coating a thin layer of protective materials on electrode materials surface has been developed as an efficient method to improve electrochemical properties of lithium-ion battery [1–3]. There are several potential advantages brought by such a surface coating, such as enhanced electric and ionic conductivity, improved materials' integrity and controllable solid electrolyte interphase (SEI) formation, *etc.* One of the potential applications of surface engineering is to develop highly reversible conversion and/or alloying reaction type electrode materials to build high-capacity and stable-cycling lithium-ion batteries [4,5]. Due to large volumetric change in cycling, the conversion/alloying reaction electrodes are easily pulverized, leading to a quick loss of capacity. A robust and reliable stronghold is needed before any conversion/alloying reaction electrodes can become practical in industry. The surface coating is normally quite thin, has a highly

disordered/amorphous structure and quite low mechanic stability (and thus is unstable in electrochemical cycles). In order to be able to use conversion/alloying reaction based materials, the amount of the additional and protective materials (such as carbon, Al_2O_3 , *etc.*) has to be greatly increased (which will lead to a reduced capacity and structural complexity thus potential problem in cycling) [6,7]. There is still lack of a reliable, thin surface coating material to be able to efficiently modify the electrode materials based on conversion/alloying reactions. Here in this work, thin N-doped carbon shell can be formed to wrap up the target electrode material by a facile method. The N-doped carbon shell has a uniform and ultrathin structure as it is directly derived from metal-organic frameworks (MOFs) and is mechanically stable.

As a new family of porous crystalline materials, MOFs are constructed by metal ions and organic linkers via coordinative bonds. MOFs possess well-defined pores, high surface areas and versatile structures, showing great potential in broad applications [8–19]. In recent years,

* Corresponding author. State Key Laboratory of Advanced Technology for Materials Synthesis and Processing, Wuhan University of Technology, Wuhan, 430070, China.

** Corresponding author.

E-mail addresses: qi.li@whut.edu.cn (Q. Li), wujs@whut.edu.cn (J. Wu).

<https://doi.org/10.1016/j.nanoen.2020.104758>

Received 26 November 2019; Received in revised form 24 March 2020; Accepted 25 March 2020

Available online 20 April 2020

2211-2855/© 2020 Elsevier Ltd. All rights reserved.

many research works have focused on investigating MOFs as precursors or templates in the preparation of MOF-derived carbon-based metal-oxide composites [17,20,21]. Despite progress made in these MOF-derived and carbon-based metal oxide materials, their morphological characteristics and chemical components are relatively unitary and highly depend on the intrinsic MOF crystals. To further endow new functionalities to MOF-derived materials, enormous efforts have been taken to develop efficient strategies to construct complex composites of MOFs with other functional materials [22–24]. Among them, the core-shell structures with functional nanostructure materials as cores and MOF as shells have attracted widespread attention [23,25,26]. To date, traditional methods of synthesizing MOF-coated composites are carried out in solutions, which involve the combination of the organic linkers and metal ions on the surface of core materials [27–29]. For example, Long et al. used metal phenolic networks thin film to bridge ZIF-8 and core materials to construct core-shell composites in the methanolic solution [30]. Despite great advancements, these synthetic methods require surface modification, involved with a large amount of solvent and many time-consuming steps such as the separation of the product and surface functionalization. Meanwhile, it is still difficult to precisely control the interfacial reaction between the core materials and the MOF layer and thus construct a uniform MOF shell. Recently, to resolve the problems, we have developed two efficient methods to realize the controllable growth of MOF shells on nanostructures by modulating the interfacial coordination reactions between solid metal precursors and gaseous/solid organic ligands in specific conditions [31]. However, because of their low reaction kinetics, the selected metal precursors must have a low bonding energy and thus can easily release metal ions to form MOF shells by coordination reactions with gaseous/solid organic ligands. Although ZnO nanostructures are employed to react with melted 2-methylimidazole, the obtained ZnO@ZIF-8 nanostructures exhibited serious aggregation and non-uniform ZIF-8 coatings due to their fast reaction kinetics, agree with those been previously reported [26]. Therefore, to develop a facile, high-yield, solvent-free and general method to realize uniform MOF coatings on most metal precursors especially those with high bonding energies is an urgent but inevitable challenge for energy-related applications.

Herein, we develop a facile, low-temperature melting method by the gradient heat treatment process to synthesize uniform and ultrathin MOF shell-derived nitrogen-doped carbon confined Zn₂SiO₄ nanowires (Zn₂SiO₄@NC). The synthetic strategy comprises of two steps: 1) the oriented growth of uniform and ultrathin MOF shell on the surface of Zn₂SiO₄ nanowires by a solid-liquid reaction and 2) the transformation from MOF shell to carbon shell by carbonization. The process is not only solvent-free, but also achieves fast reaction kinetics due to the existence of liquid melting organic ligands. The presented synthesis method is generally applicable to other ternary Zn-based oxides, such as Zn₂TiO₄ and ZnWO₄. When evaluated as a lithium-ion battery (LIB) anode material, the Zn₂SiO₄@NC nanowires showed superior cycling stability and rate performance compared to pure Zn₂SiO₄ nanowires. By *in situ* transmission electron microscopy (TEM), we have confirmed that Zn₂SiO₄ underwent conversion and alloying reaction in lithiation and Zn₂SiO₄@NC nanowires have smaller radical expansion and faster reaction kinetics than pure Zn₂SiO₄ nanowires due to existence of the mechanically robust carbon shell.

2. Experimental section

2.1. Synthesis of Zn₂SiO₄@ZIF-8 and Zn₂SiO₄@NC nanowires

Zn₂SiO₄ nanowires was prepared by a hydrothermal method. 8 mmol Zn(NO₃)₂·6H₂O was dissolved in 15 ml deionized water, and 4 mmol fumed SiO₂ was added into the prepared solution under vigorous stirring, and followed by dropwise addition of aqueous solution of NaOH (2 M) at room temperature to adjust the pH to a range of 10–11. After

stirring for 20 min, the mixed solution was loaded into 50 mL Teflon-lined autoclave, and maintained at 220 °C for 24 h. Then, the autoclave was cooled to ambient temperature. White precipitate was collected by centrifugation, washed with deionized water and ethanol, and then vacuum dried at 60 °C for 12 h. The as-prepared Zn₂SiO₄ nanowires powders and abundant 2-methylimidazole (2-MIM) powders (1:5 w/w) were grounded together in a mortar by hand for about 10 min. The homogeneous mixture was successively annealed in argon, at 180 °C for 3 h and then at 300 °C for 2 h to synthesize Zn₂SiO₄@ZIF-8 nanowires. Meanwhile, Zn₂SiO₄@NC nanowires were synthesized by successively annealing the homogeneous mixture in argon at 180 °C for 3 h firstly, then at 700 °C for 3 h.

2.2. Synthesis of ZnWO₄@ZIF-8 and ZnWO₄@NC nanorods

ZnWO₄ nanorods were prepared by a hydrothermal method. 4 mmol ZnCl₂·6H₂O and 4 mmol Na₂WO₄·2H₂O were dissolved into 35 ml deionized water, followed by dropwise addition of aqueous solution of NaOH (2 M) at room temperature until PH of solution was 10. Then, the mixed solution was put into 50 ml Teflon-lined autoclave and heated at 180 °C for 24 h. The precipitate was washed with deionized water for several times and dried at 60 °C for 12 h. The as-prepared ZnWO₄ nanorods powders and abundant 2-Methylimidazole powders (1:5 w/w) were grounded together in a mortar by hand for about 10 min. Then, ZnWO₄@ZIF-8 nanorods was obtained by the same treatment as that for Zn₂SiO₄@ZIF-8 nanowires. Finally, The ZnWO₄@NC nanorods were obtained by treating the ground mixture in argon at 180 °C for 3 h and then 700 °C for 3 h.

2.3. Synthesis of Zn₂TiO₄@ZIF-8 and Zn₂TiO₄@NC

The Zn₂TiO₄ was obtained by solid state reaction method. The 5 mmol TiO₂ powders and 2.5 mmol ZnO powders were ground in a mortar for 2 h using acetone as the medium. The grounded mixture was then calcined at 950 °C for 2 h in air. The as-prepared Zn₂TiO₄ powders and abundant 2-Methylimidazole powders (1:5 w/w) were grounded together in a mortar by hand for about 10 min. Then, Zn₂TiO₄@ZIF-8 and Zn₂TiO₄@NC were obtained by the same treatments as those for ZnWO₄@ZIF-8 and ZnWO₄@NC.

2.4. Synthesis of ZnO@ZIF-8 and ZnO@NC

The Zinc oxide powders and 2-Methylimidazole powders (1:5 w/w) were grounded together in a mortar by hand for about 10 min. The ZnO@ZIF-8 and ZnO@NC were prepared by the same treatment as those of Zn₂SiO₄@ZIF-8 and Zn₂SiO₄@NC, except that the ZnO@NC was calcined at 180 °C for 3 h and 550 °C for 3 h in argon.

2.5. Synthesis of Zn₂GeO₄@ZIF-8 and Zn₂GeO₄@NC

1 mmol Zn(Ac)₂ solution was added into 45 mL deionized water under vigorous stirring. 0.5 mmol Na₂GeO₃ was added into the prepared solution vigorous stirring for 48 h. The brown suspension was collected by centrifugation, washed with deionized water and ethanol, and then vacuum dried at 60 °C for 12 h. The as-prepared Zn₂GeO₄ nanorods powders and abundant 2-Methylimidazole powders (1:5 w/w) were grounded together in a mortar by hand for about 10 min. Then, Zn₂GeO₄@ZIF-8 nanorods was obtained by the same treatment as that for Zn₂SiO₄@ZIF-8 nanowires. Finally, The Zn₂GeO₄@NC nanorods were obtained by treating the ground mixture in argon at 180 °C for 3 h and then 700 °C for 3 h.

2.6. Characterizations

The crystallographic characteristics of the final products were measured using a Bruker D8 Discover X-ray diffractometer equipped

with a Cu $K\alpha$ radiation source. SEM images were collected using a JEOL-7100F scanning electron microscope, transmission electron microscopy (TEM), High-resolution TEM (HRTEM) images and selected-area electron diffraction (SAED) patterns were collected using a JEM-2100F transmission electron microscope. X-ray energy-dispersive spectra (EDS) were recorded using an Oxford IE250 system. In-situ TEM was performed by a TEM-STM in situ sample holder (ZepTools Co. Ltd., China) on a Thermo Fisher Tecnai TEM. Raman and Fourier-Transform Infrared Spectrometer (FTIR) spectra were obtained using a Renishaw INVIA micro-Raman spectroscopy system. X-ray Photoelectron Spectroscopy (XPS) measurements were conducted using a VG MultiLab 2000 instrument. The Brunauer Tmmett Teller (BET) surface area was calculated from nitrogen adsorption isotherms collected at 77 K using a Tristar-3020 instrument. Thermogravimetric-Differential Scanning Calorimetry (TG-DSC) analysis was conducted using an STA-449F3 instrument.

2.7. Computational details

All simulations on metal oxides were carried out by density functional theory (DFT) and the projector augmented wave method (PAW) as implemented in the Vienna *ab initio* simulation package (VASP). The exchange and correlation functional was treated as generalized gradient approximation (GGA) of the Perdew-Burke-Ernzerhof (PBE) formula. The wave functions were expanded by using the plane waves up to a kinetic energy cutoff of 520 eV. Brillouin-zone integrations were approximated by using special k -point sampling of Monkhorst-Pack scheme with a k -point mesh resolution of $2\pi * 0.02 \text{ \AA}^{-1}$. The unit cell lattice vectors (unit cell shape and size) and atomic coordinates were fully relaxed until the force on each atom was less than $0.004 \text{ eV \AA}^{-1}$.

2.8. Lithium storage measurements

The working electrode slurry were made of 70 wt% Zn_2SiO_4 @NC or Zn_2SiO_4 , 20 wt% acetylene black and 10 wt% polyvinylidene fluorides (PVDF) and N-methyl-2-pyrrolidinone (NMP). After coating onto the

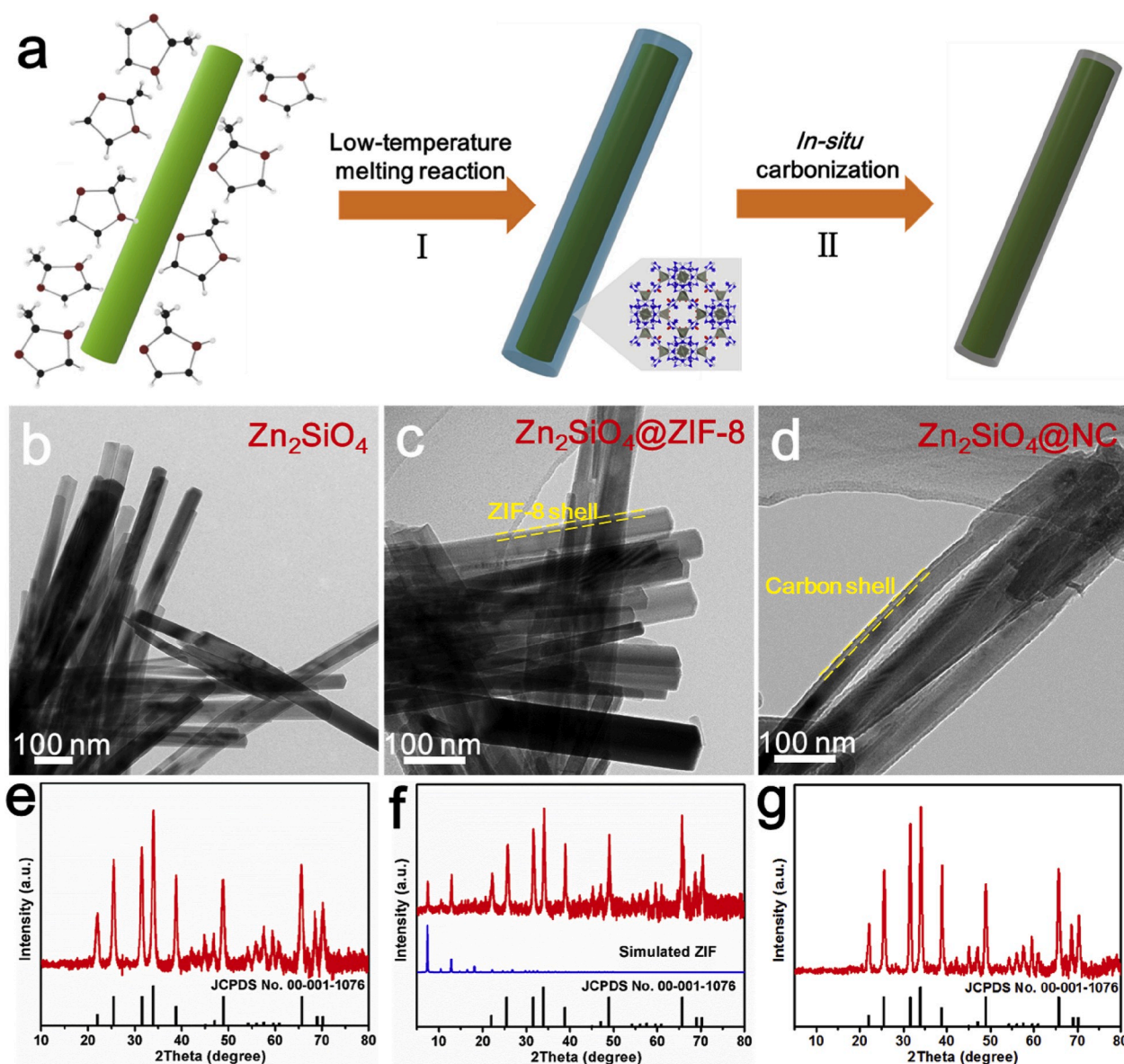


Fig. 1. (a) Schematic illustration of the formation procedure of Zn_2SiO_4 @NC nanowires. TEM images (b–d) and XRD patterns (e–g) of Zn_2SiO_4 nanowires, Zn_2SiO_4 @ZIF-8 nanowires, Zn_2SiO_4 @NC nanowires, respectively.

copper foil, the electrode film was uniformly cut into $\sim 0.78 \text{ cm}^2$ (area) round slices, weighing a total of $\sim 1 \text{ mg}$; the corresponding areal mass loading was 2 mg cm^{-2} , 016 coin cells were assembled in a glovebox filled with pure argon gas. Lithium foil was used as the counter electrode and the separator was Celgard 2400 microporous membrane. 1 M lithium hexafluorophosphate (LiPF_6) solution in ethylene carbon (EC)-dimethyl carbonate (DMC) (1:1 v/v) was used as the electrolyte. Galvanostatic charge-discharge measurements were performed using a multichannel battery testing system (LAND CT2001A). Cyclic Voltammetry (CV) and electrochemical impedance spectra were collected at room temperature using an Autolab potentiostat/galvanostat.

3. Results and discussion

The mechanism of Zn_2SiO_4 @NC nanowires' formation is shown in Fig. 1a. Zn_2SiO_4 nanowires were first synthesized by a hydrothermal method. The obtained Zn_2SiO_4 nanowires exhibit high crystallinity and uniform nanowire morphology with an average diameter of around 80 nm (Fig. 1b, e and Fig. S1). Subsequently, the mixture of Zn_2SiO_4 nanowires and 2-MIM were undertaken a gradient heat treatment in argon atmosphere, which involves two successive stages: (1) At a low temperature of 180°C , the solid 2-MIM powders as organic linkers were melted (Figs. S2 and S3). The melted 2-MIM was then reacted with Zn_2SiO_4 nanowires at the solid-liquid interface, resulting in the formation of ZIF-8 shell on their surface. During the reaction process, superficial Zn_2SiO_4 will decompose into Zn^{2+} and amorphous SiO_2 , while the inner part remains intact. The released Zn ion from Zn_2SiO_4 reacted with the melted 2-MIM to form a thin ZIF-8 layer. The surfaces of Zn_2SiO_4 nanowires show clear ZIF-8 shell (Fig. 1c and Fig. S4). In the powder X-ray diffraction (XRD) pattern, the peaks in the range of $5\text{--}25^\circ$ are well identified as the simulated ZIF-8 (Fig. 1f), confirming the formation of the ZIF-8 shell. Due to its relatively strong bond energy, the Zn ions were slowly released from Zn_2SiO_4 , guaranteeing the formation of the uniform and thin ZIF-8 shells. Furthermore, DFT calculations indicated that the bonding energy of Zn_2SiO_4 is approximately 3.77 eV, much higher than that of ZnO (2.90 eV) (Fig. S5). In contrast, when 2-MIM reacted

with ZnO nanoparticles in the same conditions, the large ZIF-8 crystals were formed on the surface of ZnO (Fig. S6). This phenomenon demonstrates that the lower bonding energy will lead to a faster reaction kinetics during the solid-liquid process. Besides, the reaction time between Zn_2SiO_4 and 2-MIM have a great impact on the growth of ZIF-8 layer. As shown in Fig. S7, for the reaction between Zn_2SiO_4 and 2-Methylimidazole at 180°C , a uniform coating is formed when the reaction time is 3 h; and when the reaction time was 6 h, the large ZIF crystal is formed around the Zn_2SiO_4 nanowires. (2) Secondly, when treated at a high temperature of 700°C , the surplus 2-MIM volatilizes and the ZIF-8 shell is *in situ* converted into the nitrogen-doped carbon shell along with the volatilization of Zn metals during the pyrolysis process. The morphology of Zn_2SiO_4 nanowires is well maintained with a uniform carbon shell on their surfaces (Fig. 1d). The powder XRD pattern of Zn_2SiO_4 @NC nanowires shows clear diffraction peaks which is in consistence with Zn_2SiO_4 , suggesting that the carbon shell has no influence on the crystalline structure of the Zn_2SiO_4 (Fig. 1g). In brief, the synthetic method comprises the oriented growth of ZIF-8 shell and *in situ* formation of carbon coating by a simple gradient heat treatment.

The structure of ZIF-8 shells on Zn_2SiO_4 nanowires after low-temperature melting reaction was further studied by electron microscopy (Fig. 2). The SEM and TEM images show uniform and delicate nanowires (Fig. 2a, b and Fig. S8a). The corresponding EDS elemental mapping shows the distribution of Zn, Si, O, N and C elements, respectively (Figs. S9a–f). From the XPS analysis, Zn_2SiO_4 @ZIF-8 nanowires exhibit newly emerged peaks of C 1s and N 1s compared with Zn_2SiO_4 nanowires, further confirming the existence of the ZIF-8 shell (Fig. S8d). HRTEM analysis further reveals that the surface of Zn_2SiO_4 nanowires are uniformly coated by the ZIF-8 shells with about 8 nm thickness (Fig. 2c and Fig. S8c). Based on FTIR analysis, the vibrational peaks of ZIF-8 crystals are also observed in the Zn_2SiO_4 @ZIF-8 nanowires (Fig. 2d), suggesting the existence of thin ZIF-8 shell. The N_2 adsorption-desorption isotherms and pore distributions of Zn_2SiO_4 @ZIF-8 and Zn_2SiO_4 are depicted in Fig. 2e and f. The specific surface area of Zn_2SiO_4 @ZIF-8 is $149.3 \text{ m}^2 \text{ g}^{-1}$, which is approximately twelve times larger than that of Zn_2SiO_4 ($11.8 \text{ m}^2 \text{ g}^{-1}$). The corresponding pore

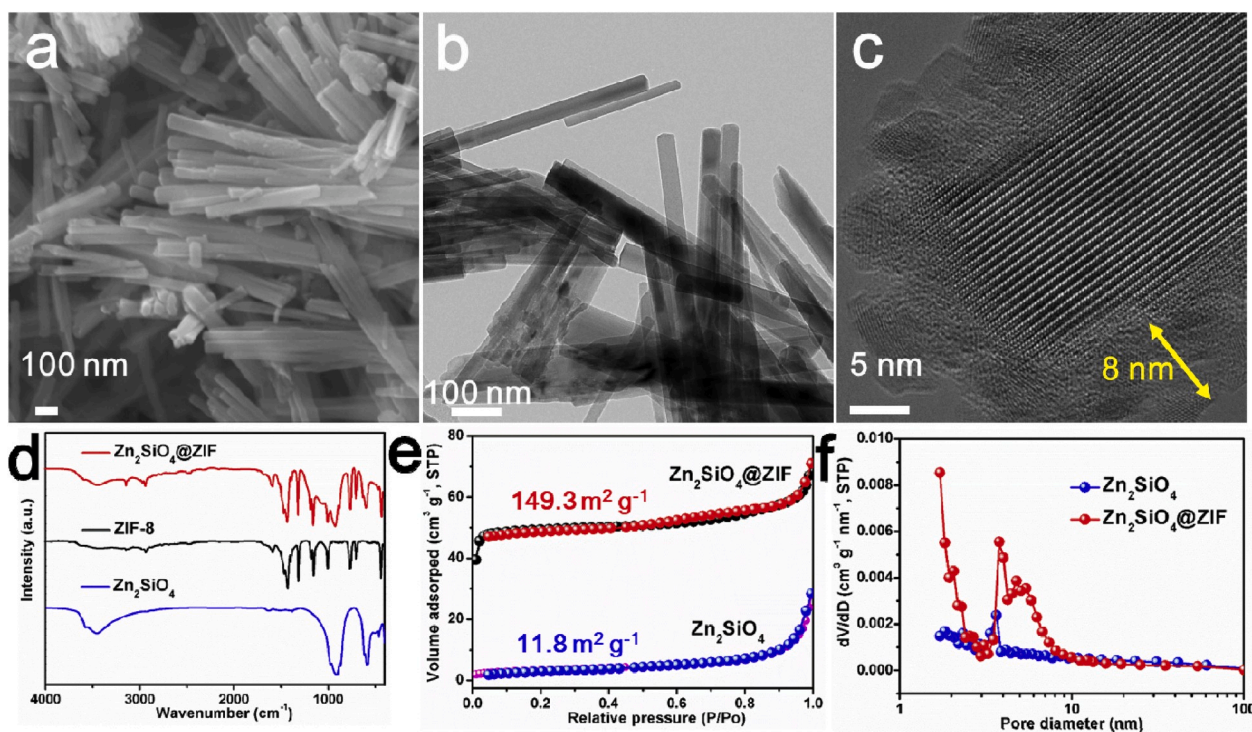


Fig. 2. SEM image (a) and TEM images (b, c) of Zn_2SiO_4 @ZIF-8 nanowires. (d) FTIR spectra of Zn_2SiO_4 @ZIF, ZIF-8 and Zn_2SiO_4 . (e, f) BET and BJH curves of Zn_2SiO_4 @ZIF and Zn_2SiO_4 .

distribution of $\text{Zn}_2\text{SiO}_4@ZIF-8$ is mainly below 2 nm and in the region between 4 and 8 nm. The micropores in $\text{Zn}_2\text{SiO}_4@ZIF-8$ exist mainly in the ZIF-8 shell.

After calcination, the structure of $\text{Zn}_2\text{SiO}_4@NC$ nanowires were also investigated by a variety of characterization methods. As shown in Fig. 3a–d, SEM and TEM images show that the morphology of $\text{Zn}_2\text{SiO}_4@NC$ nanowires is well retained. HRTEM image shows a thin continuous carbon shell of about 6 nm on a single Zn_2SiO_4 nanowire (Fig. 3e). Selected area electron diffraction pattern confirmed the single crystalline nature of Zn_2SiO_4 (Fig. 3f). The elemental mapping collected by scanning transmission electron microscopy (STEM) - EDS confirm that the Zn, Si, O, N, and C elements are uniformly distributed throughout nanowires (Fig. 3g–l). The XPS full spectrum of $\text{Zn}_2\text{SiO}_4@NC$ nanowires has clear peaks of Zn, Si, O, C, and N elements (Fig. S10c). The high-resolution N 1s XPS spectrum reveals three forms of nitrogen: graphitic N, pyrrolic N and pyridinic N (Fig. S10d). Raman spectrum of $\text{Zn}_2\text{SiO}_4@NC$ nanowires shows two obvious peaks, corresponding to D (1350 cm^{-1}) and G (1600 cm^{-1}) bands, indicating its partial graphitization (Fig. S10a) [32]. According to TG-DSC curves of $\text{Zn}_2\text{SiO}_4@NC$ nanowires, the mass fraction of carbon was calculated to be about 13% (Fig. S10b). As shown in Figs. S10e and f, the $\text{Zn}_2\text{SiO}_4@NC$ nanowires exhibit a relatively large surface area of $98.7\text{ m}^2\text{ g}^{-1}$. Pores are formed in the nitrogen-doped carbon coating and the pore size is in the mesopore range of 3–5 nm.

To testify the versatility of our strategy, we choose also ZnWO_4 nanowires and Zn_2TiO_4 nanoparticles as the precursors to synthesize

$\text{ZnWO}_4@NC$ and $\text{Zn}_2\text{TiO}_4@NC$ by this above-mentioned method. SEM images and XRD patterns show the morphologies, phase information of the obtained ZnWO_4 nanowires and Zn_2TiO_4 microparticles, respectively (Figs. S11a–c and S14a–c). After low temperature melting treatment, XRD patterns of the $\text{ZnWO}_4@ZIF-8$ nanowires and $\text{Zn}_2\text{TiO}_4@ZIF-8$ nanoparticles show that several weak diffraction peaks matched well with simulated ZIF-8, confirming the existence of ZIF-8 (Figs. S11f and S14f). TEM images directly showed uniform thin ZIF-8 shells on the surfaces (Figs. S11e and S14e). The FTIR spectra of $\text{ZnWO}_4@ZIF-8$ and $\text{Zn}_2\text{TiO}_4@ZIF-8$ show obvious vibrational peaks of ZIF-8 crystals (Figs. S13a and S16a), suggesting the existence of ZIF-8 shells. After the high-temperature pyrolysis process, $\text{ZnWO}_4@NC$ nanowires and $\text{Zn}_2\text{TiO}_4@NC$ microparticles were obtained. SEM, EDS elemental mapping and TEM images indicate the morphology-preserved nanostructures with thin carbon shells of 3–6 nm in thickness (Fig. S17). The thickness difference of carbon shells on Zn_2SiO_4 , Zn_2TiO_4 , ZnWO_4 can be attributed to their different binding energies, nanowires' diameter and surface morphology. Raman spectra further confirm the partial graphitization of derived carbon shells (Figs. S13b and S16b). Our synthesis strategy of MOF-coating will apply as long as the two conditions are satisfied: (1) the metal oxides should have a high metal-O bonding energy. If the metal-O bonding energy is low (such as ZnO), the reaction rate will be too fast, resulting in the formation of large ZIF particles on the surface (Fig. S6). (2) the metal ion in the selected metal oxides can well coordinate with 2-MIM to form MOF layer. As the other example, when the Zn_2GeO_4 nanowires was selected as precursor, $\text{Zn}_2\text{GeO}_4@ZIF$

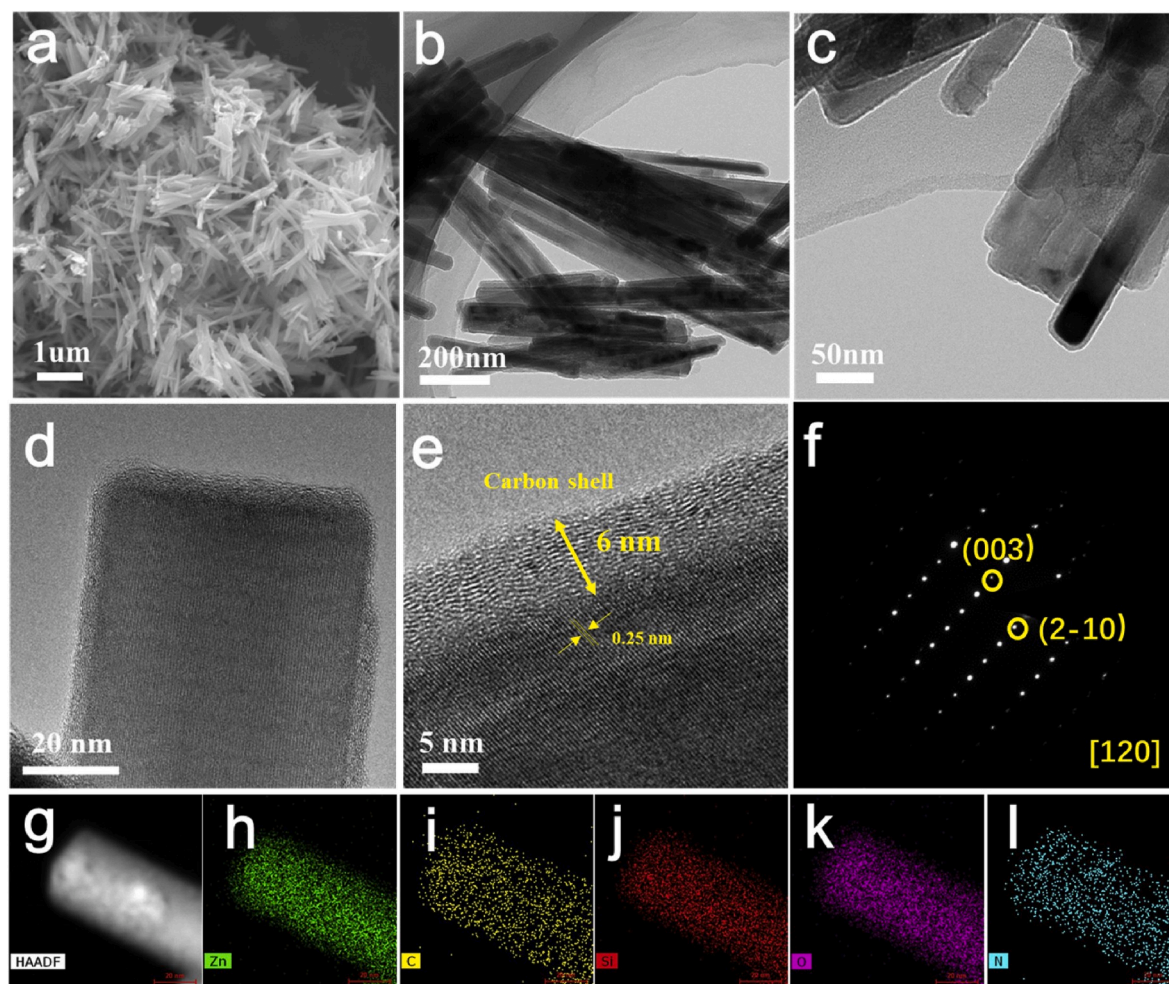


Fig. 3. Characterizations of $\text{Zn}_2\text{SiO}_4@NC$ nanowires. (a) SEM image. (b–e) TEM images. (f) SAED pattern. (g–l) TEM image and the corresponding elemental mappings.

nanowires were successfully synthesized by the low-temperature melting method, and then $\text{Zn}_2\text{GeO}_4@NC$ nanowires were successfully obtained with further high-temperature pyrolysis (Fig. S18). Therefore, the current strategy can be widely applied to other ternary nanostructured materials with a high bond energy. When previous methods are normally involved with a complicated process and nonuniform MOF-coating on substrates, here developed in the work, it is an efficient and simple method with general application in fabricating a uniform and ultrathin MOF-coating on metal oxides. As the reaction between melted 2-methylimidazole and Zn-based ternary precursors occurs locally in the

interface, the current method is solvent-free and robust in constructing a uniformly coated and ultrathin MOF shell which is difficult to form by other methods (Table S1).

As a proof-of-concept application of our obtained carbon-confined ternary metal oxide structures in energy storage, the electrochemical performances of $\text{Zn}_2\text{SiO}_4@NC$ nanowires as anode materials for LIBs have been investigated and compared with those of the pure Zn_2SiO_4 nanowires (Fig. 4). Fig. 4a shows the first four cyclic voltammograms (CV) of $\text{Zn}_2\text{SiO}_4@NC$ nanowires within the voltage window of 0.01–3 V. The first discharge process of $\text{Zn}_2\text{SiO}_4@NC$ nanowires demonstrates an

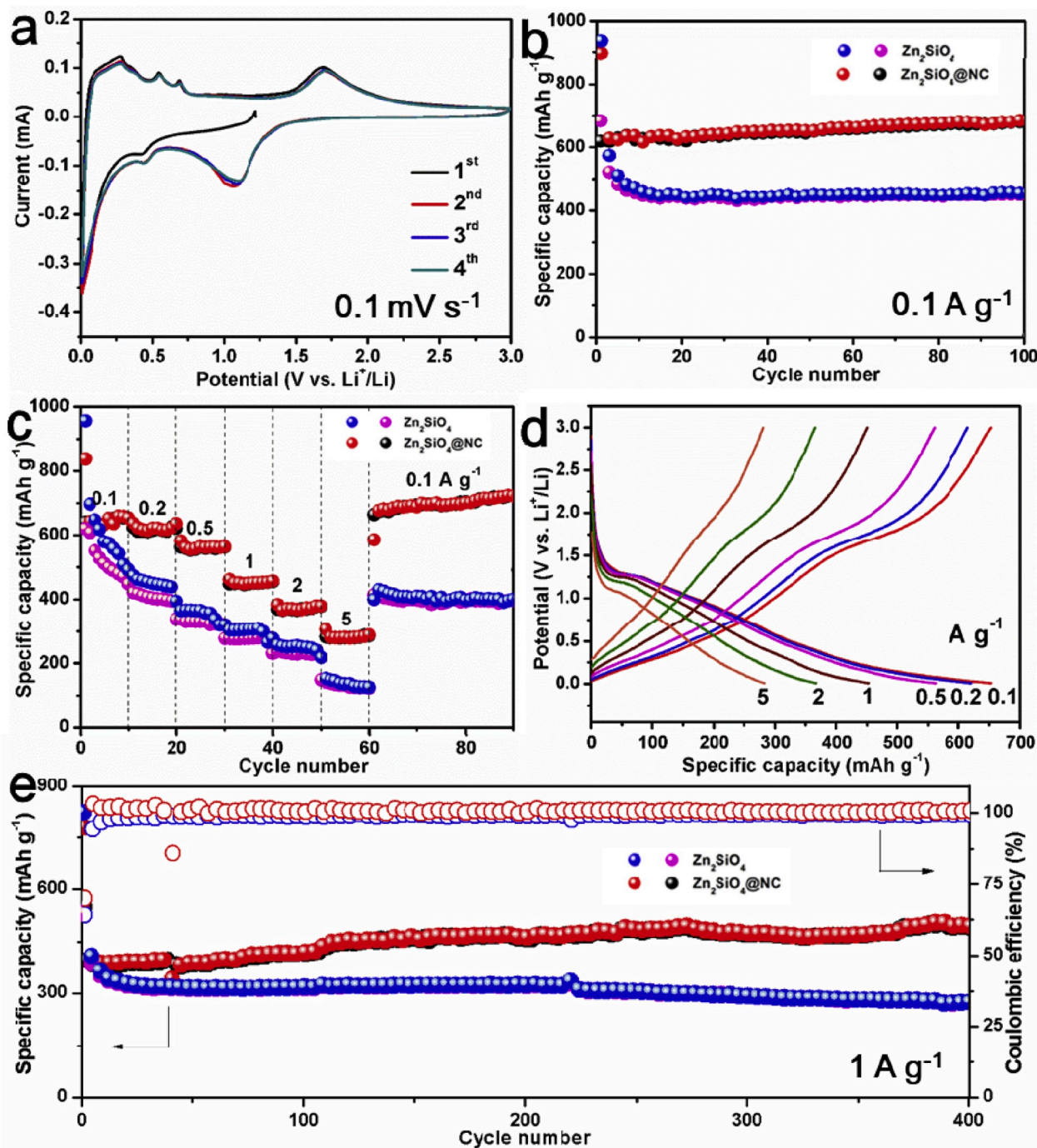


Fig. 4. Lithium storage performance of Zn_2SiO_4 nanowires and $\text{Zn}_2\text{SiO}_4@NC$ nanowires. (a) The first four CV curves of $\text{Zn}_2\text{SiO}_4@NC$ nanowires in the potential range from 0.01 to 3.0 V at a scan rate of 0.1 mV s^{-1} . (b) Cycling performance at a current density of 0.1 A g^{-1} . (c) Rate performance at various current densities from 0.1 to 5 A g^{-1} . (d) The corresponding charge and discharge voltage profiles of $\text{Zn}_2\text{SiO}_4@NC$ nanowires at different current densities. (e) Long-term cycling performance at a high current density of 1 A g^{-1} .

irreversible reduction peak at around 1.15 V, which can be attributed to the initial reduction of Zn_2SiO_4 to Zn and SiO_2 by conversion reactions [33]. The small reductive peaks at around 0.4 V can be assigned to the alloying reaction of Zn, the formation of SEI [34]. During the anodic process of the first cycle, the obvious three peaks located at 0.3, 0.5, 0.6 V can be observed, originated from the Li_xZn dealloying process [35]. The pronounced anodic peak at around 1.7 V can be ascribed to the oxidation reaction between Zn and Li_2O to form ZnO [36]. In the cathodic process of the second cycles, the existence of the sharp peak at 1.2 V may belong to the reduction of ZnO to Zn [33]. The CV curves of Zn_2SiO_4 @NC nanowires at the second cycle virtually overlap with the latter two cycle, which show high reversibility during insertion and extraction of lithium ions. Fig. 4b shows the charge/discharge cycling performances of Zn_2SiO_4 @NC nanowires and Zn_2SiO_4 nanowires at 0.1 A g^{-1} . The first discharge capacity of Zn_2SiO_4 @NC nanowires is 898.8 mAh g^{-1} , which is lower than that of Zn_2SiO_4 nanowires (935.2 mAh g^{-1}) because of the existence of low-capacity carbon coatings. After 100 cycles, Zn_2SiO_4 @NC nanowires exhibit a high discharge capacity of 685.2 mAh g^{-1} and a high capacity retention of $\sim 106\%$ compared with the second discharge capacity. In contrast, the discharge capacity of Zn_2SiO_4 nanowires decreases to 455.8 mAh g^{-1} with the capacity retention of around 70% after 100 cycles. The as-prepared Zn_2SiO_4 @NC nanowires electrode delivers enhanced rate performance compared with Zn_2SiO_4 nanowires (Fig. 4c). The high reversible specific discharge capacities of the Zn_2SiO_4 @NC are 640, 620, 560, 450, 370 and 280 mAh g^{-1} at current densities of 0.1, 0.2, 0.5, 1, 2, and 5 A g^{-1} , respectively. There is a significant difference from Fig. 4b in the charge and discharge capacity of the first circuit due to the difference in weight of electrode and open circuit voltage [31]. However, the corresponding specific capacities of the Zn_2SiO_4 nanowires are 550, 450, 350, 300, 250 and 140

mAh g^{-1} . The average discharge capacity quickly recovers to 690 mAh g^{-1} when the current density returns to 0.1 A g^{-1} . Fig. 4d and Fig. S14 show the corresponding charge and discharge voltage profiles of Zn_2SiO_4 @NC nanowires and Zn_2SiO_4 nanowires, indicating lower polarization of Zn_2SiO_4 @NC nanowires. The long-term cycling performance and the corresponding Coulombic efficiency of Zn_2SiO_4 @NC and Zn_2SiO_4 nanowires at 1 A g^{-1} has been investigated in Fig. 4e. Zn_2SiO_4 @NC nanowires electrode exhibits a higher specific capacity (540 mAh g^{-1}) after 400 cycles compared with 260 mAh g^{-1} of Zn_2SiO_4 nanowires, indicating excellent long-term cycling stability. The metallic Zn nanocrystals which are generated in the 1st cycle by the conversion of Zn_2SiO_4 have catalytic effects to facilitate the reaction between the lithiated Zn_2SiO_4 nanowires and the electrolyte in forming thick surface layers at low potential. The surface layers will also dissolve upon charge. Hence, the increasing capacity during cycling may be originated from growth and dissolution of the thick surface layer, which is different from the thin SEI layer usually formed in the first few cycles [37,38]. However, the capacity of pure Zn_2SiO_4 nanowires keep decreasing due to the structural pulverization when the carbon layer protection is lack. In addition, Zn_2SiO_4 @NC nanowires show better cycling performance compared with other transition metal silicate (Table S2) [33,39–48].

To further understand mechanism of lithiation reaction of Zn_2SiO_4 and the enhanced electrochemical performance of Zn_2SiO_4 @NC nanowires over pure Zn_2SiO_4 nanowires, *in situ* TEM was performed to study the phase transformation and morphology evolution in real time during the lithiation process (Fig. 5) [35,49–52]. Before lithiation, a pristine Zn_2SiO_4 nanowire showed its single crystalline nature, where the diffraction spots marked by red dotted ring can be indexed as closed to the [241] zone axis of Zn_2SiO_4 phase (Fig. 5a). Upon lithiation, the diffraction spots of Zn_2SiO_4 gradually disappeared and two quite

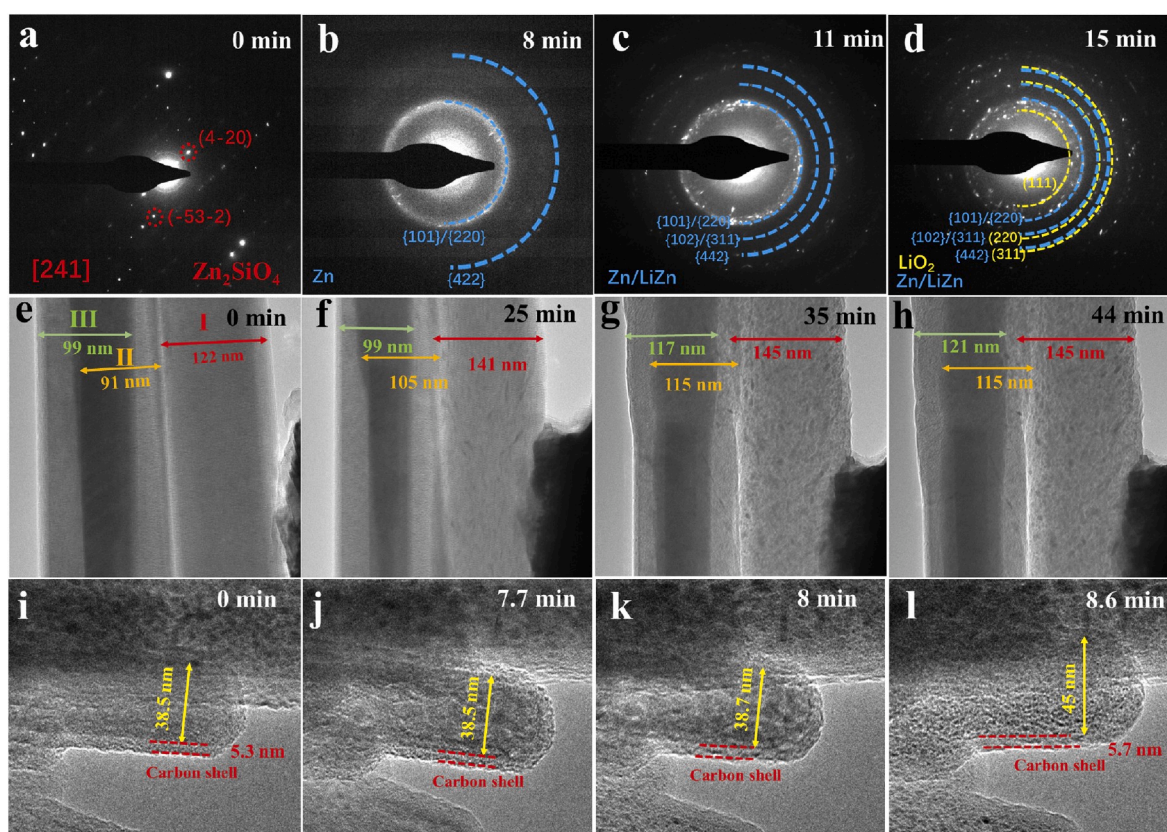
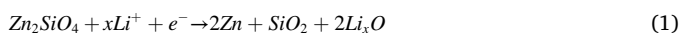


Fig. 5. Evolution of morphology and microstructure of Zn_2SiO_4 and Zn_2SiO_4 @NC nanowire. A nanobattery was designed inside TEM with Zn_2SiO_4 / Zn_2SiO_4 @NC as the cathode, lithium metal as the anode, and Li_2O grown on the surface of lithium metal as the solid electrolyte. When a bias of -10 V is applied, a lithiation process is triggered. (a–d) the dynamic electron diffraction pattern of Zn_2SiO_4 . (e–h) the morphological evolution of the Zn_2SiO_4 nanowire during lithiation reaction. (i–l) the morphological evolution of the Zn_2SiO_4 @NC nanowire during lithiation reaction.

diffused rings appeared which were corresponded mainly to faulted and polycrystalline Zn clusters with quite small size (Fig. 5b). With further lithiation, a recrystallization/crystalline growth process was observed as shown in Fig. 5c. There are clear diffraction rings which can be indexed as the Li and LiZn phases. Zn and LiZn have very closed structure and spacing in their lattice planes making it difficult to distinguish in the SAED pattern, although Zn phase will partially be transformed into Li_xZn alloy in this stage, as previously reported [19]. With further lithiation and growth of the nanocrystals, clear diffraction rings of LiO_2 , such as the {111}, {220} and {311} can be seen as shown in Fig. 5d. The above results are consistent with CV curves of $\text{Zn}_2\text{SiO}_4@\text{NC}$, showing the following electrochemical reactions in lithiation:



The morphological evolutions of the coated and uncoated nanowires upon lithiation were also analyzed. Fig. 5e–h shows the volume expansion rates of Zn_2SiO_4 nanowire (termed I, II, and III) are around 49.3%, 59.7% and 41.3% (from 99 to 121 nm, from 91 to 115 nm, and from 122 to 145 nm in diameter, respectively). By contrast, $\text{Zn}_2\text{SiO}_4@\text{NC}$ nanowires show a lower radical expansion rate of 30% (from 38.5 to 44 nm) (Fig. 5i–l). The volume expansion rate of $\text{Zn}_2\text{SiO}_4@\text{NC}$ nanowires is lower than that of pure $\text{Zn}_2\text{SiO}_4@\text{NC}$ nanowires. Meanwhile, the speed of lithiation reaction of the $\text{Zn}_2\text{SiO}_4@\text{NC}$ nanowires is faster than that of the Zn_2SiO_4 nanowires. For the $\text{Zn}_2\text{SiO}_4@\text{NC}$ nanowire (I), it took only ~ 8.6 min to expand from 38.5 nm to 44 nm. Due to the $\text{Zn}_2\text{SiO}_4@\text{NC}$ nanowire (I) observed by *in situ* TEM indirectly contacted to bulk metallic Li, the lithium ion should take some time to transport into the $\text{Zn}_2\text{SiO}_4@\text{NC}$ nanowire. Besides, since the $\text{Zn}_2\text{SiO}_4@\text{NC}$ nanowire is coated with a uniform carbon layer, the lithium ions should diffuse through the coating before they can react with the Zn_2SiO_4 . Hence, in the first ~ 8 min, before the Li-ions' diffusion path was established, very little volume expansion was observed. However, when the carbon shell expanded from 5.3 nm to 5.7 nm right after ~ 8 min, the reaction was accelerated resulting in a large volumetric expansion of the nanowire. Meanwhile, even with the large expansion, the intimate connection between the lithiated carbon shell with the lithiated mixtures of Li_xZn , SiO_2 and Li_2O remains intact. The tightly coated carbon in lithiation provides not only high electric conductivity to speed up the lithiation reaction rate, but also a strong host to suppress the unstable SEI and materials pulverization.”

$\text{Zn}_2\text{SiO}_4@\text{NC}$ nanowires exhibit superior electrochemical performance over pure Zn_2SiO_4 nanowires, which can be ascribed to the following aspects. First, the high specific surface area ($98.7 \text{ m}^2 \text{ g}^{-1}$) increase the exposing of the electrode to the electrolyte and thus enhance the diffusion of lithium ions. Second, the existence of N-doped carbon shell can improve the electronic conductivity. As shown by the *in situ* TEM study, the lithiation rate of $\text{Zn}_2\text{SiO}_4@\text{NC}$ nanowires is faster than that of Zn_2SiO_4 nanowires. Also, the electrochemical impedance spectroscopy (EIS) plot (Fig. S20b) shows that $\text{Zn}_2\text{SiO}_4@\text{NC}$ nanowires have a lower charge-transfer resistance of 20Ω than Zn_2SiO_4 nanowires (38Ω), indicating a fast electronic mobility. Third, the strong and robust N-doped carbon shell on the surface of Zn_2SiO_4 nanowires can buffer the volume expansion and thus improve the structure stability during cycling (Fig. S21). Therefore, the well-designed MOF-derived carbon coatings endow nanostructured electrodes with enhanced rate capability and good cycling stability, displaying great potential in energy storage devices.

4. Conclusion

In summary, for the first time, a facile and scalable approach has been developed to synthesize uniform and ultrathin MOF shell-derived carbon confined nanostructures via a well-designed gradient heat treatment process. The formation mechanism is clearly revealed by

various characterizations and analyses. During the heat treatment process, MOF shells *in situ* forms on the surfaces of selected nanostructured precursors under low-temperature melting condition through coordination reaction, and then carbonizes at high-temperature pyrolysis to form a carbon shell. This represents a general method which will be widely applicable to other nanostructured materials. Compared with pure Zn_2SiO_4 nanowires, the obtained $\text{Zn}_2\text{SiO}_4@\text{NC}$ nanowires exhibit superior lithium storage performance. Specifically, tested at 0.1 A g^{-1} after 100 cycles, these $\text{Zn}_2\text{SiO}_4@\text{NC}$ nanowires displayed a highly reversible capacity of 685.2 mAh g^{-1} with the capacity retention of 106%. *In situ* TEM was performed to reveal mechanism of lithiation reaction of Zn_2SiO_4 and confirm $\text{Zn}_2\text{SiO}_4@\text{NC}$ nanowires have lower expansion rate and higher reaction kinetics than Zn_2SiO_4 nanowires. The synthetic method will open new avenues for the design of MOF-assisted nanostructures in many frontier applications.

Declaration of competing interest

The authors declare that they have no known competing financial interests or personal relationships that could have appeared to influence the work reported in this paper.

Acknowledgements

This work was supported by the National Natural Science Fund for Distinguished Young Scholars (51425204), the National Natural Science Foundation of China (51302203, 21805219), the National Key R&D Program of China (2016YFA0202603), the Programme of Introducing Talents of Discipline to Universities (B17034), the Yellow Crane Talent (Science & Technology) Program of Wuhan City and the Fundamental Research Funds for the Central Universities (WUT: 2019III012GX, 2017III009, 2017IVA100, 2017IVA096, 2017III040). This S/TEM work was performed at the Nanostructure Research Center (NRC), which is supported by the State Key Laboratory of Advanced Technology for Materials Synthesis and Processing, and the State Key Laboratory of Silicate Materials for Architectures (all of the laboratories are at Wuhan University of Technology).

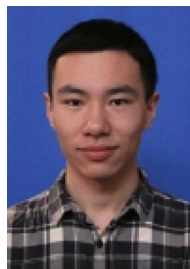
Appendix A. Supplementary data

Supplementary data to this article can be found online at <https://doi.org/10.1016/j.nanoen.2020.104758>.

References

- [1] B.N. Yun, H.L. Du, J.Y. Hwang, H.G. Jung, Y.K. Sun, *J. Mater. Chem.* 5 (2017) 2802–2810.
- [2] K.X. Wang, X.H. Li, J.S. Chen, *Adv. Mater.* 27 (2015) 527–545.
- [3] W.M. Zhang, X.L. Wu, J.S. Hu, Y.G. Guo, L.J. Wan, *Adv. Funct. Mater.* 18 (2010) 3941–3946.
- [4] H. Liu, Z. He, L. Lei, S. Jia, M. Shuang, C. Fan, Y. Lv, D. Zhao, J. Wang, *Adv. Mater. Interfaces* 5 (2018) 1701255.
- [5] Z. Lu, Z. Zhang, X. Chen, Q. Chen, F. Ren, M. Wang, S. Wu, P. Zhe, D. Wang, J. Ye, *Energy Storage Mater.* 11 (2018) 47–56.
- [6] X. Wang, K. Chen, G. Wang, X. Liu, H. Wang, *ACS Nano* 11 (2017) 11602–11616.
- [7] L. Zhou, H.B. Wu, Z. Wang, X.W. Lou, *ACS Appl. Mater. Interfaces* 3 (2011) 4853–4857.
- [8] A.J. Howarth, Y. Liu, P. Li, Z. Li, T.C. Wang, J.T. Hupp, O.K. Farha, *Nat. Rev. Mater.* 1 (2016) 1–15.
- [9] S.T. Meek, J.A. Greathouse, M.D. Allendorf, *Adv. Mater.* 23 (2011) 249–267.
- [10] D. Yuan, D. Zhao, D. Sun, H.C. Zhou, *Angew. Chem. Int. Ed.* 49 (2010) 5357–5361.
- [11] E. Virmani, J.M. Rotter, A. Mahringer, T. von Zons, A. Godt, T. Bein, S. Wuttke, D. D. Medina, *J. Am. Chem. Soc.* 140 (2018) 4812–4819.
- [12] J. Jiang, Y. Zhao, O.M. Yaghi, *J. Am. Chem. Soc.* 138 (2016) 3255–3265.
- [13] Y. Zheng, S.-Z. Qiao, *Inside Chem.* 2 (2017) 751–752.
- [14] S.-L. Li, Q. Xu, *Energy Environ. Sci.* 6 (2013) 1656–1683.
- [15] J. Liu, L. Chen, H. Cui, J. Zhang, L. Zhang, C.Y. Su, *Chem. Soc. Rev.* 43 (2014) 6011–6061.
- [16] A. Schoedel, Z. Ji, O.M. Yaghi, *Nat. Energy* 1 (2016) 1–13.
- [17] W. Xia, A. Mahmood, R. Zou, Q. Xu, *Energy Environ. Sci.* 8 (2015) 1837–1866.
- [18] J. Meng, C. Niu, L. Xu, J. Li, X. Liu, X. Wang, Y. Wu, X. Xu, W. Chen, Q. Li, Z. Zhu, D. Zhao, L. Mai, *J. Am. Chem. Soc.* 139 (2017) 8212–8221.

- [19] I. Stassen, N. Campagnol, J. Fransaeer, P. Vereecken, D. Vosaand R. Ameloot, *CrystEngComm* 15 (2013) 9308–9311.
- [20] F. Zou, Y.M. Chen, K. Liu, Z. Yu, W. Liang, S.M. Bhoway, M. Gao, Y. Zhu, *ACS Nano* 10 (2016) 377–386.
- [21] Y.T. Xu, X. Xiao, Z.M. Ye, S. Zhao, R. Shen, C.T. He, J.P. Zhang, Y. Li, X.M. Chen, *J. Am. Chem. Soc.* 139 (2017) 5285–5288.
- [22] X. Huang, B. Zheng, Z. Liu, C. Tan, J. Liu, B. Chen, H. Li, J. Chen, X. Zhang, Z. Fan, *ACS Nano* 8 (2014) 8695–8701.
- [23] J.Y. Zeng, X.S. Wang, M.K. Zhang, Z.H. Li, D. Gong, P. Pan, L. Huang, S.X. Cheng, H. Cheng, X.Z. Zhang, *ACS Appl. Mater. Interfaces* 9 (2017) 43143–43153.
- [24] G. Zhang, S. Hou, H. Zhang, W. Zeng, F. Yan, C.C. Li, H. Duan, *Adv. Mater.* 27 (2015) 2400–2405.
- [25] J. Zhou, P. Wang, C. Wang, T.G. Yi, Z. Fang, P.B. Messersmith, H. Duan, *ACS Nano* 9 (2015) 6951–6960.
- [26] Q. Ganab, K. Zhaoab, S.Z. He, *Electrochim. Acta* 250 (2017) 292–301.
- [27] X. Liu, L. He, J. Zheng, J. Guo, F. Bi, X. Ma, K. Zhao, Y. Liu, R. Song, Z. Tang, *Adv. Mater.* 27 (2015) 3273–3277.
- [28] W. Zhang, Z.Y. Wu, H.L. Jiang, S.H. Yu, *J. Am. Chem. Soc.* 136 (2014) 14385–14388.
- [29] G. Huang, D.M. Yin, L.M. Wang, *J. Mater. Chem.* 4 (2016) 15106–15116.
- [30] Y. Long, L. Xiao, Q. Cao, X. Shi, Y. Wang, *Chem. Commun.* 53 (2017) 10831–10834.
- [31] J. Meng, X. Liu, J. Li, Q. Li, C. Zhao, L. Xu, X. Wang, F. Liu, W. Yang, X. Xu, Z. Liu, C. Niu, L. Mai, *Nano Lett.* 17 (2017) 7773–7781.
- [32] Z. Xiao, J. Meng, Q. Li, X. Wang, M. Huang, Z. Liu, C. Han, L. Mai, *Sci. Bull.* 63 (2018) 46–53.
- [33] S. Zhang, L. Ren, S. Peng, *CrystEngComm* 16 (2014) 6195–6202.
- [34] H. Fan, H. Yu, Y. Zhang, J. Guo, Z. Wang, H. Wang, X. Hao, N. Zhao, H. Geng, Z. Dai, Q. Yan, J. Xu, *Nano Energy* 33 (2017) 168–176.
- [35] X. An, H. Yang, Y. Wang, Y. Tang, S. Liang, A. Pan, G. Cao, *Sci. China Mater.* 60 (2017) 717–727.
- [36] Y. Wang, X. Jiang, L. Yang, N. Jia, Y. Ding, *ACS Appl. Mater. Interfaces* 6 (2014) 1525–1532.
- [37] H. Kim, W. Choi, J. Yoon, J. Um, W. Lee, J. Kim, J. Cabana, W. Yoon, *Chem. Rev.* (2020). <http://doi:10.1021/acs.chemrev.9b00618>.
- [38] B. Zhang, Y. Zhang, Z. Miao, T. Wu, Z. Zhang, X. Yang, *J. Power Sources* 248 (2014) 289–295.
- [39] P. Guo, C. Wang, *RSC Adv.* 5 (2015) 70661–70667.
- [40] S. Zhang, L.L. Hou, M. Hou, H. Liang, *Mater. Lett.* 156 (2015) 82–85.
- [41] Z. Sun, Y. Li, Z. Yi, J. Zhou, W. Min, Y. Meng, X. Zhao, L. Ma, *J. Mater. Sci.* 29 (2018) 7867–7875.
- [42] P. Guo, C. Wang, *RSC Adv.* 7 (2017) 4437–4443.
- [43] Z. Fan, Y. An, Z. Wei, X. Gao, J. Feng, L. Ci, S. Xiong, *Mater. Res. Bull.* 70 (2015) 573–578.
- [44] Q.Q. Wang, J. Qu, Y. Liu, C.X. Gui, S.M. Hao, Y. Yu, Z.Z. Yu, *Nanoscale* 7 (2015) 16805–16811.
- [45] W. Cheng, F. Rechberger, G. Ilari, H. Ma, W.I. Lind, M. Niederberger, *Chem. Sci.* 6 (2015) 6908–6915.
- [46] C. Gui, S.M. Hao, Y. Liu, J. Qu*, C. Yang, Y. Yu, Q. Wang, Z. Yu, *J. Mater. Chem.* 3 (2015) 16551–16559.
- [47] R. Jin, Y. Yang, Y. Li, X. Liu, Y. Xing, S. Song, Z. Shi, *Chem. Eur J.* 21 (2015) 9014–9017.
- [48] X. Chen, Y. Huang, K. Zhang, *J. Colloid Interface Sci.* 513 (2018) 788–796.
- [49] H.J. Yu, Z. Li, W.C. Min, J.P. Sullivan, X. Wu, Z.L. Qiang, S.X. Mao, N.S. Hudak, L. X. Hua, S. Arunkumar, *Science* 42 (2011) 1515–1520.
- [50] Q. Li, H. Liu, Z. Yao, J. Cheng, T. Li, Y. Li, C. Wolverton, J. Wu, V.P. Dravid, *ACS Nano* 10 (2016) 8788–8795.
- [51] Q. Li, J. Wu, Z. Yao, Y. Xu, M.M. Thackeray, C. Wolverton, V.P. Dravid, *Nano Energy* 44 (2018) 15–22.
- [52] Q. Li, Z. Yao, J. Wu, S. Mitra, S. Hao, T.S. Sahu, Y. Li, C. Wolverton, V.P. Dravid, *Nano Energy* 38 (2017) 342–349.



Shiyu Liu has being an undergraduate student and in Department of Materials Science and Engineering at Wuhan University of Technology since 2015. His current research focuses on the electrochemical energy storage materials and devices.



Jiashen Meng received his B.S. degree from Wuhan University of Technology in 2015. He is currently working toward the Ph.D degree in Wuhan University of Technology. From 2018 to 2019, he was a visiting student at the department of materials science and engineering at MIT. His current research focuses on the energy conversion and storage materials.



Fanjie Xia is a postgraduate at State Key Laboratory of Advanced Technology for Materials Synthesis and Processing and Nanostructure Research Centre, Wuhan University of Technology. He received his BS degree in Materials Chemistry from Wuhan Polytechnic University. He currently works on TEM and STEM based technique development and applications in materials science.



Zhitong Xiao received his B.S. degree in Material Science and Engineering from Jinan University in 2016. He is currently working toward the Ph.D. degree in Materials Science and Engineering from Wuhan University of Technology. His current research focuses on the layered cathode materials of potassium-ion batteries.



Fang Liu obtained her mater degree in Materials Science and Engineering from Wuhan University of Technology in 2019. She is currently working toward the Ph.D. degree in Materials Science and Engineering at Wuhan University of Technology. Her current research focuses on *in situ* TEM and STEM based technique development and applications in energy storage materials.



Ziang Liu received his B.Sc. degree from Wuhan University of Technology in 2017. He is currently a Ph.D. candidate under the supervision of Prof. Liqiang Mai in State Key Laboratory of Advanced Technology for Materials synthesis and Processing. He is working on the electrospinning fabricating one-dimensional nanostructure for high energy-density battery.



Qi Li is an Associate Professor at Wuhan University of Technology (WUT). She received her B.Sc. (1999) and M.Sc. (2002) degrees from Peking University, and Ph.D. (2007) from the University of Melbourne under the supervision of Prof. Frank Caruso. After graduation, she worked as a postdoctoral research fellow for a few years with Prof. Alan Bond at Monash University before joining WUT in 2016. Her current research interests focus on the rational design of nano energy materials in particular via controlled assembly for electrochemical energy storage and conversion.



Liqiang Mai is Changjiang Scholar Chair Professor of Materials Science and Engineering at Wuhan University of Technology (WUT). He is the winner of the National Natural Science Fund for Distinguished Young Scholars and Fellow of the Royal Society of Chemistry. He received his Ph.D. from WUT in 2004 and carried out his postdoctoral research with Prof. Zhong Lin Wang at Georgia Institute of Technology in 2006–2007. He worked as an advanced research scholar with Prof. Charles M. Lieber at Harvard University in 2008–2011 and Prof. Peidong Yang at University of California, Berkeley in 2017. His current research interests focus on new nanomaterials for electrochemical energy storage and micro/nano energy devices.



Jinsong Wu is currently a professor and executive director of Nanostructure Research Centre at Wuhan University of Technology. He earned his Ph.D. degree from the Department of Materials Science and Engineering at Dalian University of Technology in 1998. He had worked in Juelich Research Center in Germany (1999-2001), Arizona State University (2001-2006) and Northwestern University in the USA (2007-2018) as an electron microscopist. Dr. Wu's research interests include transmission electron microscopy, electron tomography, in-situ transmission electron microscopy and nanomaterials for energy storage.